

Journal of Materials Chemistry A

Accepted Manuscript



This is an *Accepted Manuscript*, which has been through the Royal Society of Chemistry peer review process and has been accepted for publication.

Accepted Manuscripts are published online shortly after acceptance, before technical editing, formatting and proof reading. Using this free service, authors can make their results available to the community, in citable form, before we publish the edited article. We will replace this *Accepted Manuscript* with the edited and formatted *Advance Article* as soon as it is available.

You can find more information about *Accepted Manuscripts* in the [Information for Authors](#).

Please note that technical editing may introduce minor changes to the text and/or graphics, which may alter content. The journal's standard [Terms & Conditions](#) and the [Ethical guidelines](#) still apply. In no event shall the Royal Society of Chemistry be held responsible for any errors or omissions in this *Accepted Manuscript* or any consequences arising from the use of any information it contains.

[001] preferentially-oriented 2D tungsten disulfide nanosheets as anode materials for superior lithium storage

Wanfeng Yang,^a Jiawei Wang,^b Conghui Si,^a Zhangquan Peng,^b Jan Frenzel,^c Gunther Eggeler,^c Zhonghua Zhang^{*a}

^aKey Laboratory for Liquid-Solid Structural Evolution and Processing of Materials (Ministry of Education), School of Materials Science and Engineering, Shandong University, Jingshi Road 17923, Jinan, 250061, P.R. China

^bState Key Laboratory of Electroanalytical Chemistry, Changchun Institute of Applied Chemistry, Chinese Academy of Sciences, Changchun, Jilin 130022, P.R. China

^cInstitut für Werkstoffe, Ruhr Universität Bochum, Bochum 44780, Germany

*Corresponding author. Email: zh_zhang@sdu.edu.cn (Z. Zhang), [Tel/Fax: +86-531-88396978](tel:+86-531-88396978).

Abstract

Rechargeable lithium ion batteries (LIBs) have transformed portable electronics and will play a crucial role in transportation like electric vehicles. For higher energy storage in LIBs, two issues should be addressed, that is, fundamental understanding of the chemistry taking place in LIBs and discovery of new materials. Here we design and fabricate two-dimensional (2D) WS₂ nanosheets with preferential orientation of [001] and perfect single crystalline structures. Being used as an anode for LIBs, the WS₂-nanosheet electrode exhibits high specific capacity, good cycling performance and excellent rate capability. Considering the controversy in the lithium storage mechanism of WS₂, ex-situ X-ray diffraction (XRD), Raman and X-ray photoelectron spectroscopy (XPS) analyses clearly verify that the recharge product (3.0 V vs. Li⁺/Li) of the WS₂ electrode after fully discharging to 0.01 V (vs. Li⁺/Li) tends to reverse to

WS₂. More remarkably, the [001] preferentially-oriented 2D WS₂ nanosheets are also promising candidates for applications in photocatalysis, water splitting, and so forth.

Introduction

Rechargeable lithium ion batteries (LIBs) are one of the most desirable approaches to alleviate energy shortage and global climate warming issues which the world is currently facing.¹⁻⁵ High energy and power densities are of great essential to LIBs for applications in electric vehicles, stationary energy storage systems for solar and wind energy as well as smart grid.⁶⁻⁸ Because the conventional electrodes of LIBs are inadequate to fulfill these requirements, developing new materials and novel composites with excellent electrochemical performances are critical for next generation LIBs.⁹⁻¹¹

Very recently, the layer structured transition metal dichalcogenides (TMDs) with strong in-plane covalent bonds and weak out-of-plane van der Waals forces have attracted significant attention due to their immense potentials for various applications.¹²⁻¹⁵ Among TMDs, two dimensional (2D) nanoscale metal disulfides, such as MoS₂ and WS₂, have been intensively studied to examine their properties, including electrical transport,¹⁶⁻¹⁹ luminescence,²⁰⁻²² photocurrent and catalytic properties,²³⁻²⁵ as well as their strain effects.²⁶ Owing to the similar feature of the layered structure as graphite, 2D metal disulfides could have a great potential for alternative anode materials.²⁷⁻²⁹ As a representative, MoS₂ has already received great

scientific interest as the anode for LIBs and significant improvement in cycle life and rate performance has been achieved thanks to the numerous efforts devoted to promoting the low intrinsic electrical conductivity.³⁰⁻³³ In comparison, WS₂ seems to be a more suitable candidate as the lithium ion anode due to its higher intrinsic electric conductivity than MoS₂. Besides, WS₂ has a larger spacing between neighboring (002) planes (6.18 Å) than that of graphite (3.35 Å), which in principle may make Li⁺ diffuse easier. And its 4-electron transfer reaction when hosting lithium ions enables its lithium storage capacity (443 mA h g⁻¹) higher than that of the commercial graphite anode (372 mA h g⁻¹).^{28,34} Moreover, the density of WS₂ is 7.6 g cm⁻³, resulting in high volumetric energy density (about 4 times over graphite). For example, layered WS₂ supported on reduced graphene oxide delivered a capacity of about 400-450 mA h g⁻¹ after 50 cycles at 100 mA g⁻¹, with a relatively low initial coulombic efficiency of 48%.³⁵ Tungsten sulfide-carbon composite microspheres were also synthesized by spray pyrolysis, which exhibited a capacity of 555 mA h g⁻¹ at the 50th cycle.³⁶ However, as a qualified anode material for high performance LIBs, further investigations are needed to be done for searching novel fabrication methods and improving the rate capability and cycling stability of WS₂. In addition, Wang et al. recently reported that the end products when WS₂ discharged to 0.01 V (vs. Li⁺/Li) were metallic W and Li₂S while the recharge (3.00 V vs. Li⁺/Li) products were metallic W and S,³⁷ inconsistent with many other literatures which reported that the recharge products reversed to WS₂.^{38,39} It is essential to further explore its lithium storage mechanism.

As is known, nanomaterials have the genuine potential to make a significant impact on the performance of LIBs, as their reduced dimensions enable high intercalation/deintercalation rates. The physical and chemical properties of nanostructured materials depend crucially on their morphologies and sizes. Therefore, nanomaterials have been widely explored to improve the electrochemical performance of LIBs, including 0D quantum dots,⁴⁰ 1D nanoribbons,⁴¹ 2D nanosheets,³⁹ and 3D nanomaterials.⁴² Herein, we fabricate the [001] preferentially-oriented 2D WS₂ nanosheets with perfect single crystal structures. As the anode for LIBs, the WS₂-nanosheet electrode achieves a stable reversible capacity of about 539.1 mA h g⁻¹ after 60 cycles at a current density of 0.2 A g⁻¹ and a high rate capability. Considering the controversy in the lithium storage mechanism of WS₂, ex-situ XRD, Raman and XPS analyses verify that the recharge product (3.0 V vs. Li⁺/Li) of the WS₂ electrode after fully discharging to 0.01 V (vs. Li⁺/Li) tends to reverse to WS₂. More importantly, the [001] preferentially-oriented 2D WS₂ nanosheets with perfect single crystal structures could have immense potentials in other fields, for example, photocatalysis and hydrogen evolution reactions.^{25,43}

Experimental section

Fabrication of preferentially-oriented 2D WS₂ nanosheets

The [001] preferentially-oriented 2D WS₂ nanosheets were fabricated by calcination of metallic W and S powders. The mixture of W and S powders (purity: 99.9 wt. %) with the atomic ratio of 1:2.1 was sealed in a vacuum quartz tube, and

then treated in a resistance furnace at 155 °C for 3 hours. At the temperature, the molten S with the lowest viscosity could easily wet the metallic W. Then, the temperature was increased to and kept at 600 °C for 10 hours. After cooling down to room temperature, the 2D WS₂ nanosheets were obtained without further treatment.

Morphological and structural characterization

The X-ray diffraction (XRD) patterns of the as-prepared and discharged/charged samples were determined by a XD-3 diffractometer (Beijing Purkinje General Instrument Co., Ltd, China) equipped with Cu K α radiation. The morphology and microstructure of WS₂ nanosheets were characterized using a scanning electron microscope (SEM, LEO 1530 VP), together with a transmission electron microscope (TEM, FEI Tecnai G2). Additionally, selected-area electron diffraction (SAED) pattern was obtained to document the crystalline nature of the as-prepared samples. The scanning transmission electron microscopy (STEM) images were also obtained under high angle annular dark field (HAADF) mode. The acceleration voltage for TEM and STEM measurements is 200 KV. Besides, the chemical compositions of the as-prepared samples were determined by energy dispersive X-ray spectroscopy (EDX) in the SEM and nanobeam-EDX (NB-EDX) by the FEI Tecnai G2 microscope under the HAADF mode. Further evidence for the composition of the product was achieved by X-ray photoelectron spectroscopy (XPS) which was carried out at room temperature with ESCALAB 250 spectrometer and monochromatic Al K α X-ray source (150 W). All reported binding energy values are calibrated to the C 1s peak at 284.8 eV. For the ex-situ XRD and Raman testing, cells were cycled to the required

voltage and opened. The cycled electrodes were washed with dimethyl carbonate (DMC) solution to remove the lithium salt before testing. Raman spectroscopy was performed by a LabRAM HR Evolution Raman system (HORIBA Scientific, $\lambda=633$ nm). In addition, the UV-vis diffuse reflectance spectra (DRS) were recorded in a wavelength range of 250-800 nm.

Electrochemical measurement

The as-obtained WS₂-nanosheet anode slurry was created by mixing 80 wt. % active material, 10 wt. % acetylene black (Super-P), and 10 wt. % polyvinylidene fluoride (PVDF) binder dissolved in N-methyl-2-pyrrolidinone (NMP) solvent. The working electrodes were produced by coating the slurry on Cu foil (thickness: 9 μm) and drying at 120 °C for 12 h. The galvanostatic discharging/charging tests were conducted using standard 2032 type coin cells with a lithium foil as both the counter electrode and reference electrode, a polypropylene (PP) film (Celgard 2325) as the separator, and 1.0 M LiPF₆ in mixed ethylene carbonate (EC) and DMC (EC:DMC, 1:1 by volume) as the electrolyte. The CR2032-type coin cells were assembled in an argon-filled glove box with oxygen and moisture levels below 1 ppm, and galvanostatically cycled at different current densities between 0.01 and 3.00 V (vs. Li⁺/Li) by using a LAND-CT2001A test system. Cyclic voltammetry (CV) was measured on a CHI660E potentiostat at a scan rate of 0.1 mV s⁻¹ over a potential window of 0.01-3.00 V (vs. Li⁺/Li). Electrochemical impedance spectroscopy (EIS) measurements were conducted with the CHI660E potentiostat in the charged state (3 V vs. Li⁺/Li). The frequency was from 0.01 Hz to 100 kHz with an excitation voltage

of 5 mV.

Results and discussion

XRD pattern of the as-prepared WS₂ samples is presented in **Figure 1a**. The spectrum shows highly crystalline hexagonal structure. All the diffraction peaks could be indexed to pure phase of WS₂ (P63/mmc space group, JCPDS NO. 08-0237, 2H-WS₂) without any peaks of W and S phases. Additionally, the EDX results demonstrate that the as-prepared powders are composed of W and S (**Figure 1b**). It is noteworthy that the intensity of the (002) diffraction peak is extraordinarily higher than that of other peaks, suggesting that the WS₂ samples are dominantly exposed to the crystal plane of (002) (inset of **Figure 1a**). The morphology of the as-obtained WS₂ powders was visualized by the SEM images (**Figure 1c** and **Figure S1**). The WS₂ samples are nanosheets with various sizes. And the diameter of the nanosheets is around 0.1-2 μm while the thickness is 20-50 nm (**Figure 1c** and **Figure S1b**). Furthermore, the zoom-in SEM image (**Figure 1c**) shows that the nanosheets are formed by stacking several thinner lamellar WS₂ nanosheets along the same crystal plane of (002), as illustrated in **Figure 1d**.

The morphology and crystal structure of the WS₂ samples were further clarified by TEM observation and electron diffraction (**Figure 2** and **Figure S2**). The bright-field TEM images of the WS₂ nanosheets in **Figure 2a**, **b** and **Figure S2a** verify that the nanosheets with the thickness of ~ 15 nm stack along the same crystal plane to form relatively thick ones. The HRTEM image in **Figure S2b** shows two

monolayers without any defects. **Figure S2c** also shows the perfect crystal structure of WS₂ although a nanosheet stacks on the other one. The SAED pattern in **Figure 2c** confirms the formation of WS₂, and the diffraction spots were unequivocally indexed to 2H-WS₂ (JCPDS NO. 08-0237). The SAED results indicate the perfect single crystalline nature of the WS₂ nanosheets. The normal direction to the dominantly exposed crystal planes (hexagon surface) is the [001] axis, which is coincident with the direction of the electron beam. The HRTEM image and fast Fourier transform (FFT) analysis (**Figure 2d**) further confirm the hexagonal lattice structure and the single crystalline feature of WS₂. The magnified HRTEM image (**Figure 2e**) shows a lattice spacing of 2.75 Å assigned to the (100) planes whereby the clear hexagonal rings are formed of W atoms (**Figure 2f**). Additionally, a STEM image of the as-obtained WS₂ in **Figure 2g** presents the 2D nanosheet structures and several single nanosheets overlap along the dominantly exposed planes, in well agreement with the bright-field TEM images. The NB-EDX analysis (**Figure 2h, i**) indicates that both the stacking regions and single nanosheet only consist of W and S atoms (the Cu signals come from the supporting Cu mesh). The above results demonstrate that we have obtained high-quality WS₂ nanosheets with preferential orientation of [001].

The XPS spectra before and after surface etching by Ar⁺ sputtering were performed to analyze the bonding characteristics and surface composition of the as-obtained WS₂ nanosheets as presented in **Figure 3** and **Figure S3**, respectively. Peaks at 32.8, 35.0, and 38.4 eV are ascribed to W 4f_{7/2}, W 4f_{5/2}, and W 5p_{5/2}, respectively (**Figure 3a**), with spin-orbit splitting of $\Delta E_p (4f_{5/2}-4f_{7/2}) = 2.2$ eV. As for

the peak at 36.3 eV in **Figure 3a**, which was swept away through the surface etching (**Figure S3c**), we assign it to the W-O bond, indicating a low surface oxidation. The peaks of S 2p_{3/2} and S 2p_{1/2} orbital of divalent sulfide ions are observed at 162.5 and 163.7 eV, respectively (**Figure 3b**). The bonding energy of the elements is consistent with the W⁴⁺ and S²⁻ in WS₂,^{43,44} further confirming the formation of pure WS₂ phase.

In this work, the 2D WS₂ nanosheets were used as an anode material for LIBs. Its working mechanism for lithium storage was investigated firstly by the combination of electrochemical measurement, ex-situ XRD, Raman and XPS analyses (**Figure 4**). **Figure 4a** shows the discharge/charge profile for the initial cycle of the WS₂-nanosheet electrode at 10 mA g⁻¹ between 0.01 and 3.0 V (vs. Li⁺/Li). Several typical cells were selected at different states, as the letters “a” to “h” denoted in **Figure 4a**, for ex-situ measurements. As the discharging process goes ahead, the intensity of the (002) diffraction peak decreases gradually, suggesting that WS₂ reacts with Li⁺ constantly (**Figure 4b**). In comparison to the original electrode before cycling, no obvious diffraction peaks except Cu were detected at the states of “g” and “h” (**Figure 4c**), which may be attributed to the nanoscale dispersion and the degraded crystallinity of the redox products.^{45,46} In the discharge process, the reduction products of WS₂ at 0.01 V (vs. Li⁺/Li) could be assigned to metallic W and amorphous Li₂S, as reported in the literatures.^{37,38} Li₂S and metals are the most-common discharge products of transition-metal sulfides, such as MoS₂, FeS, and NiS.^{32,47} Upon Raman analysis, we see that the Raman spectrum of pristine WS₂ electrode is featured by two sharp peaks at 351 cm⁻¹ and 416 cm⁻¹, corresponding to

the in-plane E2g vibration and the out-of-plane A1g vibration respectively, as well as several weak peaks marked by rectangles (**Figure 4d**). Similar to the ex-situ XRD results, the intensity of E2g and A1g vibrations diminishes and the peaks in rectangles disappear with the cells discharging (**Figure 4d**). Noticeably, when the cell recharges to 3.0 V (vs. Li⁺/Li), the vanished peaks reemerge, confirming the recovery of WS₂ (**Figure 4d**). Besides, the positions of E2g and A1g vibrations slightly shift to 349 cm⁻¹ and 414 cm⁻¹ respectively, which could be attributed to structural or textural modifications during the first lithiation process.

In order to further clarify the working mechanism of WS₂, XPS surface analyses of the electrode at the state of “g” and “h” were carried out in the same test conditions. From the XPS broad scan spectra in **Figure S4**, the same element species can be detected at both states. High-resolution XPS spectra of W 4f and S 2p in the full discharge (0.01 V vs. Li⁺/Li) and charge (3 V vs. Li⁺/Li) states were given in **Figure 4e-h**. The weak peak at 29.4 eV indicates the presence of W⁰⁺ while the two intensive peaks at 35.4 eV and 37.5 eV correspond to W⁶⁺, which may be ascribed to the easy surface oxidation of nano-sized W⁰⁺ (**Figure 4e**). Compared with the XPS spectrum of W after fully-discharging, the peak for W⁰⁺ disappears while the intensity of W⁴⁺ peaks (32.6 and 34.8 eV) increases in the fully-charging state (**Figure 4g**), indicating the reversible conversion reaction mechanism. Moreover, the two peaks at 162.1 eV and 163.2 eV in **Figure 4f** correspond to S²⁻, whereas the peaks at 166.9 eV and 169.0 eV are assigned to S⁶⁺, implying the inevitable surface oxidation of S²⁻.^{43,48} Similarly, after the 1st charge to 3 V (vs. Li⁺/Li), the distribution of the peak locations was

almost changeless, demonstrating that the valence of S maintains constant during the discharge/charge process except the unavoidable surface oxidation (**Figure 4h**). As a result, the reduction products of WS₂ at 0.01 V (vs. Li⁺/Li) could be assigned to metallic W and Li₂S and the recharge product tends to be WS₂ reversibly. Therefore, the redox reaction of lithium ions with the WS₂-nanosheet electrode can be summarized as: $WS_2 + 4 Li^+ + 4 e^- \leftrightarrow W + 2Li_2S$.

The CV measurement has also been measured to reveal the electrochemical reaction mechanism. **Figure 5a, b** shows the CV curves from the WS₂-nanosheet electrode at a scan rate of 0.1 mV s⁻¹ over a voltage window of 0.01-3.00 V (vs. Li⁺/Li). As shown in **Figure 5a**, the first five CV profiles of the WS₂-nanosheet electrode are similar except for the first scan. A strong cathodic peak located at around 0.56 V (vs. Li⁺/Li) can be observed in the first cycle, which is ascribed to the reduction of WS₂ to metallic W embedded in a Li₂S matrix accompanying the decomposition of the electrolyte.^{35,49} The anodic peak at 2.43 V (vs. Li⁺/Li) is accounted for the oxidation of W to WS₂.³⁸ From the 2nd cycle, the original reduction peak at 0.56 V (vs. Li⁺/Li) disappears while two smaller cathodic peaks appear at 2.06 V and 1.84 V (vs. Li⁺/Li), which corresponds to the formation of Li_xWS₂ upon the lithium insertion into WS₂, suggesting the dramatic lithium driven, structural or textural modifications during the first lithiation process.^{38,50} After 20 galvanostatic discharge/charge cycles at 0.2 A g⁻¹, the peak positions and current of the following CV scans are still similar to those of the initial five cycles, showing excellent electrochemical reversibility and cycling stability of the WS₂-nanosheet electrode

(Figure 5b).

Figure 5c presents the potential versus capacity profiles in the 1st, 2nd, 10th, 30th and 60th cycles of the WS₂-nanosheet electrode at 0.2 A g⁻¹ between 0.01 and 3.0 V (vs. Li⁺/Li). In the first discharge process, the potential decreases dramatically, followed by a plateau at 0.7 V (vs. Li⁺/Li), corresponding to the reduction of WS₂ and the decomposition of the electrolyte.³⁵ In the subsequent cycles, the much higher and more sloping discharge plateaus located at 2.0 V (vs. Li⁺/Li) can be observed, indicating the easier Li⁺ insertion in the successive cycles. The charge plateaus located at about 2.3 V (vs. Li⁺/Li) represent the reverse reaction for the formation of WS₂.³⁸ These results are in good accordance with the CV measurement.

Cyclic performance of the WS₂-nanosheet electrode at current densities of 0.2 A g⁻¹ and 1 A g⁻¹ is displayed in Figure 5d and e, respectively. The first discharge/charge capacity at 0.2 A g⁻¹ is 904.6/700.9 mA h g⁻¹ with a Coulombic efficiency of 77.5% (Figure 5d), which is much higher than most of the previous literatures as presented in Table S1.^{35,36,38,39,49,51-53} The irreversible capacity during the first cycle may result from different reasons, such as the formation of the solid electrolyte interface (SEI) layer and the organic conductive polymer, as well as the electrolyte decomposition.⁵⁴ The WS₂-nanosheet electrode delivers the 10th discharge/charge capacity of 632.2/617.1 mA h g⁻¹, corresponding to a Coulombic efficiency of 97.6%. After 10 cycles, the specific capacity of the WS₂-nanosheet electrode tends to be stable. The reversible capacity maintains 539.1 mA h g⁻¹ after the 60th cycle, with 87.4% retention compared to that of the 10th cycle (Figure 5d). Figure 5e exhibits an ultralong cycling

stability with a capacity retention of 193.7 mA h g⁻¹ over 1000 cycles at a high current density of 1 A g⁻¹, proving its excellent tolerance of ultrafast insertion and extraction of lithium ions for long-life LIBs. The presently reported electrochemical performance of the WS₂-nanosheet electrode is superior to that of other WS₂ electrodes previously reported. For example, the surface-functionalized WS₂ nanosheet electrode delivered a much lower reversible capacity of 118 mA h g⁻¹ after 50 cycles at an extremely low current density of 25 mA g⁻¹.⁵⁵ Besides, WS₂ supported on reduced graphene oxide exhibited an initial Coulombic efficiency of 48% and maintained a relatively low specific capacity of 400-450 mA h g⁻¹ even at the aid of graphene.³⁵ The excellent cyclability of the present WS₂-nanosheet anode can be attributed to 2D layer structured WS₂ with the perfect single crystalline nature, which can provide short diffusion paths for lithium ions and allow efficient ingress and infiltration of the electrolyte into the electrode.^{36,56}

The rate performance of the WS₂-nanosheet electrode was measured at varying current densities (**Figure 6**). With increasing current densities, the separation between the discharge plateaus and charge plateaus are enlarged due to the dynamic limitation, rendering higher overpotentials (**Figure 6a**).⁵⁷ The WS₂-nanosheet electrode delivers a specific capacity of 634.2 mA h g⁻¹ at a current density of 0.1 A g⁻¹ after 10 cycles, and the reversible capacity remains as high as 552, 484.6, 410.9 and 321 mA h g⁻¹, decreasing regularly with increasing current densities of 0.2, 0.4, 0.8 and 1.6 A g⁻¹ respectively (**Figure 6b**). Remarkably, when the current density returns to 0.1 A g⁻¹, the electrode could recover its capacity to about 541.7 mA h g⁻¹, indicating that the

WS₂-nanosheet electrode has good structural stability and rate performance.

EIS was employed to in-depth understand the lithiation/delithiation processes at the electrode/electrolyte interface. And the data of Nyquist plots (**Figure 7a**) before cycling and after 20 cycles were analyzed by fitting to equivalent circuits as **Figure 7b** and **Figure 7c**, respectively. The intercept on the Z real axis corresponds to the electrolyte resistance (R_e). The semicircle in the high and middle frequency regions is due to the presence of SEI resistance (R_{sei}) combined with the charge-transfer resistance (R_{ct}) for the transfer of Li⁺ across the SEI to the electrode. An inclined line at low frequency is in relation to the Warburg impedance (Z_w) of the Li⁺ diffusion in the solid materials. The resistance values obtained from the impedance spectra are summarized in **Table S2**. The similar intercept on the Z real axis of the 0th (3.3 Ω) and 20th (4.2 Ω) cycles shows that the WS₂-nanosheet electrode possesses a low and stable electrolyte resistance. After electrochemical reaction, the value of R_{sei} is 6.6 Ω , which can be changeless after the SEI film formed in the initial cycle. Apparently, the radius of the semicircle decreases drastically, indicating the sharp decrease of R_{ct} from 135.6 Ω (the 0th cycle) to 29.6 Ω (the 20th cycle), which can be attributed to the significant structural change from submicro-sized WS₂ to nano-sized metallic W and Li₂S matrix in the first reduction reaction. The onset of conversion processes associated with Li⁺ insertion kinetics could be observed by the reduction of the initially broad semicircle upon cycling.

It should be noted that the lithium storage is just one potential application of the present preferentially oriented WS₂ nanosheets. On one hand, we could further

improve the reversible capacity, rate capability and long-term cycling performance of WS₂ through combination with carbon materials such as graphene, carbon nanotubes (CNTs), or exfoliation of WS₂ nanosheets into thinner films. On the other hand, the present WS₂ nanosheets with special orientation could find wide applications in other fields like photocatalysis, water splitting, and so forth. It is known that P25 TiO₂ is the state-of-the-art photocatalyst for solar cells and photodegradation of organic pollutants, but mainly responds to ultraviolet (UV) irradiation, **Figure S5**. It is urgent to enhance the visible light response of photocatalysts. The UV-vis DRS results (**Figure S5**) demonstrate that the present WS₂ nanosheets exhibit strong absorption of both UV and visible light (250-800 nm), indicating their potential applications as photocatalysts.

Conclusions

In summary, the [001] preferentially-oriented 2D WS₂ nanosheets can be synthesized by calcination of metallic W and S powders. The layer structured WS₂ nanosheets possess dominantly exposed (002) crystal planes and perfect single crystalline nature. When being applied as a lithium ion anode, the 2D WS₂-nanosheet electrode exhibits high specific capacity, good cycling performance and high rate capability. Additionally, ex-situ XRD, Raman and XPS analyses clearly verify that the recharge product (3.0 V vs. Li⁺/Li) of the WS₂ electrode after fully discharging to 0.01 V (vs. Li⁺/Li) tends to reverse to WS₂. More remarkably, the [001] preferentially-oriented 2D WS₂ nanosheets with perfect single crystal structures show

great potentials for applications in photocatalysis, water splitting, and so forth.

Acknowledgements

We acknowledge the financial support from the National Natural Science Foundation of China (51371106), Specialized Research Fund for the Doctoral Program of Higher Education of China (20120131110017), and Young Top Talent Support Project (the Organization Department of the Central Committee of the CPC). The Institute of Materials of Ruhr University Bochum is acknowledged for the support of SEM and TEM characterization. Z.H. Zhang also acknowledges the financial support of the Alexander von Humboldt Foundation (Germany).

References

1. B. Dunn, H. Kamath and J.-M. Tarascon, *Science*, 2011, **334**, 928-935.
2. B. Scrosati and J. Garche, *J. Power Sources*, 2010, **195**, 2419-2430.
3. Z. Yang, J. Zhang, M. C. W. Kintner-Meyer, X. Lu, D. Choi, J. P. Lemmon and J. Liu, *Chem. Rev.*, 2011, **111**, 3577-3613.
4. P. Simon and Y. Gogotsi, *Nat. Mater.*, 2008, **7**, 845-854.
5. J.-M. Tarascon and M. Armand, *Nature*, 2001, **414**, 359-367.
6. B. Kang and G. Ceder, *Nature*, 2009, **458**, 190-193.
7. B. C. Melot and J. M. Tarascon, *Acc. Chem. Res.*, 2013, **46**, 1226-1238.
8. F. Cheng, J. Liang, Z. Tao and J. Chen, *Adv. Mater.*, 2011, **23**, 1695-1715.
9. C. Masarapu, V. Subramanian, H. Zhu and B. Wei, *Adv. Funct. Mater.*, 2009, **19**, 1008-1014.
10. Y. Zhao, X. Li, B. Yan, D. Li, S. Lawes and X. Sun, *J. Power Sources*, 2015, **274**, 869-884.
11. X. Li and C. Wang, *J. Mater. Chem., A*, 2013, **1**, 165-182.
12. Q. H. Wang, K. Kalantar-Zadeh, A. Kis, J. N. Coleman and M. S. Strano, *Nat. Nanotech.*, 2012, **7**, 699-712.
13. H. S. S. Ramakrishna Matte, A. Gomathi, A. K. Manna, D. J. Late, R. Datta, S. K. Pati and C. N. R. Rao, *Angew. Chem.*, 2010, **122**, 4153-4156.
14. M. Chhowalla, H. S. Shin, G. Eda, L.-J. Li, K. P. Loh and H. Zhang, *Nat.*

- Chem.*, 2013, **5**, 263-275.
15. K. S. Novoselov, D. Jiang, F. Schedin, T. J. Booth, V. V. Khotkevich, S. V. Morozov and A. K. Geim, *Proc. Nat. Acad. Sci. U. S. A.*, 2005, **102**, 10451-10453.
 16. C. Zhang, Z. Ning, Y. Liu, T. Xu, Y. Guo, A. Zak, Z. Zhang, S. Wang, R. Tenne and Q. Chen, *Appl. Phys. Lett.*, 2012, **101**, 113112.
 17. R. Levi, O. Bitton, G. Leitun, R. Tenne and E. Joselevich, *Nano Lett.*, 2013, **13**, 3736-3741.
 18. B. W. H. Baugher, H. O. H. Churchill, Y. Yang and P. Jarillo-Herrero, *Nano Lett.*, 2013, **13**, 4212-4216.
 19. RadisavljevicB, RadenovicA, BrivioJ, GiacomettiV and KisA, *Nat. Nanotech.*, 2011, **6**, 147-150.
 20. R. S. Sundaram, M. Engel, A. Lombardo, R. Krupke, A. C. Ferrari, P. Avouris and M. Steiner, *Nano Lett.*, 2013, **13**, 1416-1421.
 21. G. Eda, H. Yamaguchi, D. Voiry, T. Fujita, M. Chen and M. Chhowalla, *Nano Lett.*, 2011, **11**, 5111-5116.
 22. H. R. Gutiérrez, N. Perea-López, A. L. Elías, A. Berkdemir, B. Wang, R. Lv, F. López-Urías, V. H. Crespi, H. Terrones and M. Terrones, *Nano Lett.*, 2013, **13**, 3447-3454.
 23. N. Perea-López, A. L. Elías, A. Berkdemir, A. Castro-Beltran, H. R. Gutiérrez, S. Feng, R. Lv, T. Hayashi, F. López-Urías, S. Ghosh, B. Muchharla, S. Talapatra, H. Terrones and M. Terrones, *Adv. Funct. Mater.*, 2013, **23**,

- 5511-5517.
24. H. S. Lee, S.-W. Min, Y.-G. Chang, M. K. Park, T. Nam, H. Kim, J. H. Kim, S. Ryu and S. Im, *Nano Lett.*, 2012, **12**, 3695-3700.
 25. D. Voiry, H. Yamaguchi, J. Li, R. Silva, D. C. B. Alves, T. Fujita, M. Chen, T. Asefa, V. B. Shenoy, G. Eda and M. Chhowalla, *Nat. Mater.*, 2013, **12**, 850-855.
 26. P. Lu, X. Wu, W. Guo and X. C. Zeng, *Phys. Chem. Chem. Phys.*, 2012, **14**, 13035-13040.
 27. J. Zhou, J. Qin, X. Zhang, C. Shi, E. Liu, N. Zhao and C. He, *ACS Nano*, 2015, **9**, 3837-3848.
 28. R. Chen, T. Zhao, W. Wu, F. Wu, L. Li, J. Qian, R. Xu, H. Wu, H. M. Albishri and A. S. Al-Bogami, *Nano Lett.*, 2014, **14**, 5899-5904.
 29. J.-w. Seo, J.-t. Jang, S.-w. Park, C. Kim, B. Park and J. Cheon, *Adv. Mater.*, 2008, **20**, 4269-4273.
 30. C. Zhu, X. Mu, P. A. van Aken, Y. Yu and J. Maier, *Angew. Chem. Int. Ed.*, 2014, **53**, 2152-2156.
 31. C. Lu, W.-w. Liu, H. Li and B. K. Tay, *Chem. Commun.*, 2014, **50**, 3338-3340.
 32. C. Wang, W. Wan, Y. Huang, J. Chen, H. H. Zhou and X. X. Zhang, *Nanoscale*, 2014, **6**, 5351-5358.
 33. P. Sun, W. Zhang, X. Hu, L. Yuan and Y. Huang, *J. Mater. Chem. A*, 2014, **2**, 3498-3504.
 34. B. Qu, C. Ma, G. Ji, C. Xu, J. Xu, Y. S. Meng, T. Wang and J. Y. Lee, *Adv.*

- Mater.*, 2014, **26**, 3854-3859.
35. K. Shiva, H. R. Matte, H. Rajendra, A. J. Bhattacharyya and C. Rao, *Nano Energy*, 2013, **2**, 787-793.
 36. S. H. Choi, S. J. Boo, J.-H. Lee and Y. C. Kang, *Sci. Rep.*, 2014, **4**, 5755.
 37. X. Fang, C. Hua, C. Wu, X. Wang, L. Shen, Q. Kong, J. Wang, Y. Hu, Z. Wang and L. Chen, *Chem. Eur. J.*, 2013, **19**, 5694-5700.
 38. Y. Liu, W. Wang, H. Huang, L. Gu, Y. Wang and X. Peng, *Chem. Commun.*, 2014, **50**, 4485-4488.
 39. Y. Liu, W. Wang, Y. Wang and X. Peng, *Nano Energy*, 2014, **7**, 25-32.
 40. R. Mo, Z. Lei, K. Sun and D. Rooney, *Adv. Mater.*, 2014, **26**, 2084-2088.
 41. L. Li, A.-R. O. Raji and J. M. Tour, *Adv. Mater.*, 2013, **25**, 6298-6302.
 42. Y. Yu, L. Gu, X. Lang, C. Zhu, T. Fujita, M. Chen and J. Maier, *Adv. Mater.*, 2011, **23**, 2443-2447.
 43. Y. Sang, Z. Zhao, M. Zhao, P. Hao, Y. Leng and H. Liu, *Adv. Mater.*, 2015, **27**, 363-369.
 44. X. Mao, Y. Xu, Q. Xue, W. Wang and D. Gao, *Nanoscale Res. Lett.*, 2013, **8**, 1-6.
 45. X. Wang, X. Shen, Z. Wang, R. Yu and L. Chen, *ACS Nano*, 2014, **8**, 11394-11400.
 46. X. Fang, X. Guo, Y. Mao, C. Hua, L. Shen, Y. Hu, Z. Wang, F. Wu and L. Chen, *Chem. Asian J.*, 2012, **7**, 1013-1017.
 47. Y. Kim and J. B. Goodenough, *J. Phys. Chem. C*, 2008, **112**, 15060-15064.

48. J. Kim and Y. Han, *Met. Mater. Int.*, 2014, **20**, 571-575.
49. D. Chen, G. Ji, B. Ding, Y. Ma, B. Qu, W. Chen and J. Y. Lee, *Nanoscale*, 2013, **5**, 7890-7896.
50. S. Grugeon, S. Laruelle, R. Herrera-Urbina, L. Dupont, P. Poizot and J. Tarascon, *J. Electrochem. Soc.*, 2001, **148**, A285-A292.
51. W. Lv, J. Xiang, F. Wen, Z. Jia, R. Yang, B. Xu, D. Yu, J. He and Z. Liu, *Electrochim. Acta*, 2015, **153**, 49-54.
52. R. Chen, T. Zhao, W. Wu, F. Wu, L. Li, J. Qian, R. Xu, H. Wu, H. M. Albishri, A. S. Al-Bogami, D. Abd El-Hady, J. Lu and K. Amine, *Nano Lett.*, 2014, **14**, 5899-5904.
53. X. Xu, C. S. Rout, J. Yang, R. Cao, P. Oh, H. S. Shin and J. Cho, *J. Mater. Chem. A*, 2013, **1**, 14548-14554.
54. Y. Liu, W. Wang, Y. Wang and X. Peng, *Nano Energy*, 2014, **7**, 25-32.
55. R. Bhandavat, L. David and G. Singh, *J. Phys. Chem. Lett.*, 2012, **3**, 1523-1530.
56. H. Liu, D. Su, G. Wang and S. Z. Qiao, *J. Mater. Chem.*, 2012, **22**, 17437-17440.
57. H.-W. Lee, P. Muralidharan, R. Ruffo, C. M. Mari, Y. Cui and D. K. Kim, *Nano Lett.*, 2010, **10**, 3852-3856.

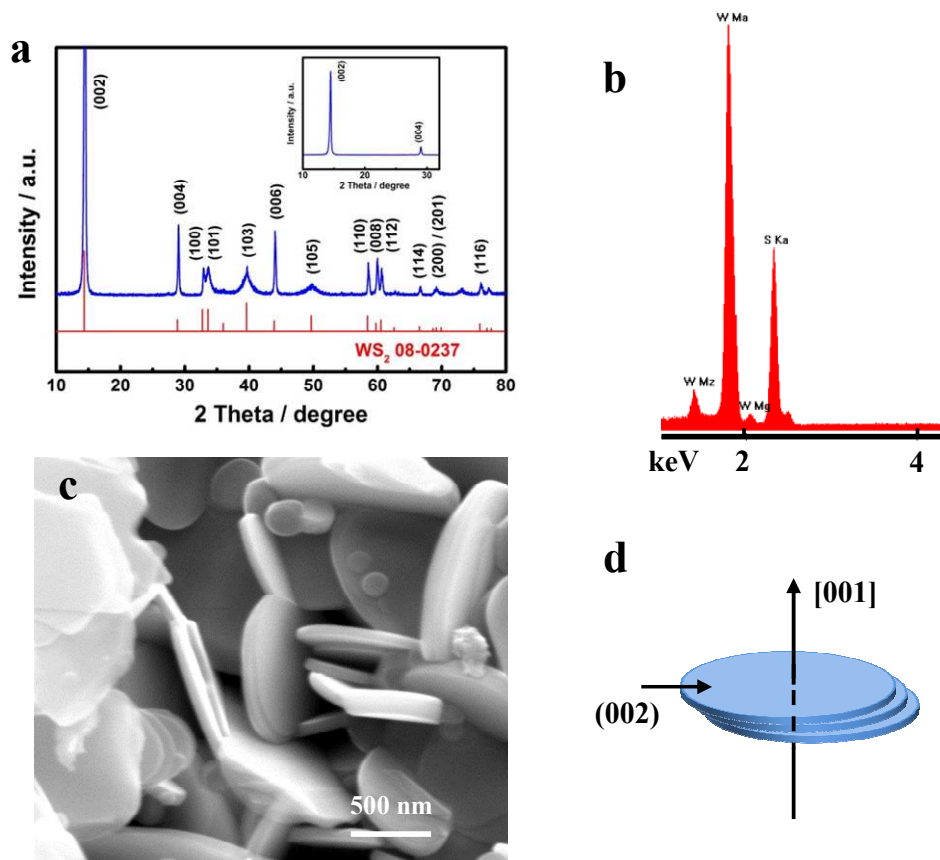


Figure 1. (a) XRD pattern, (b) EDX image, (c) SEM image of the WS₂ nanosheets. (d) Schematic illustration of the layer-like structure and crystalline orientation of WS₂.

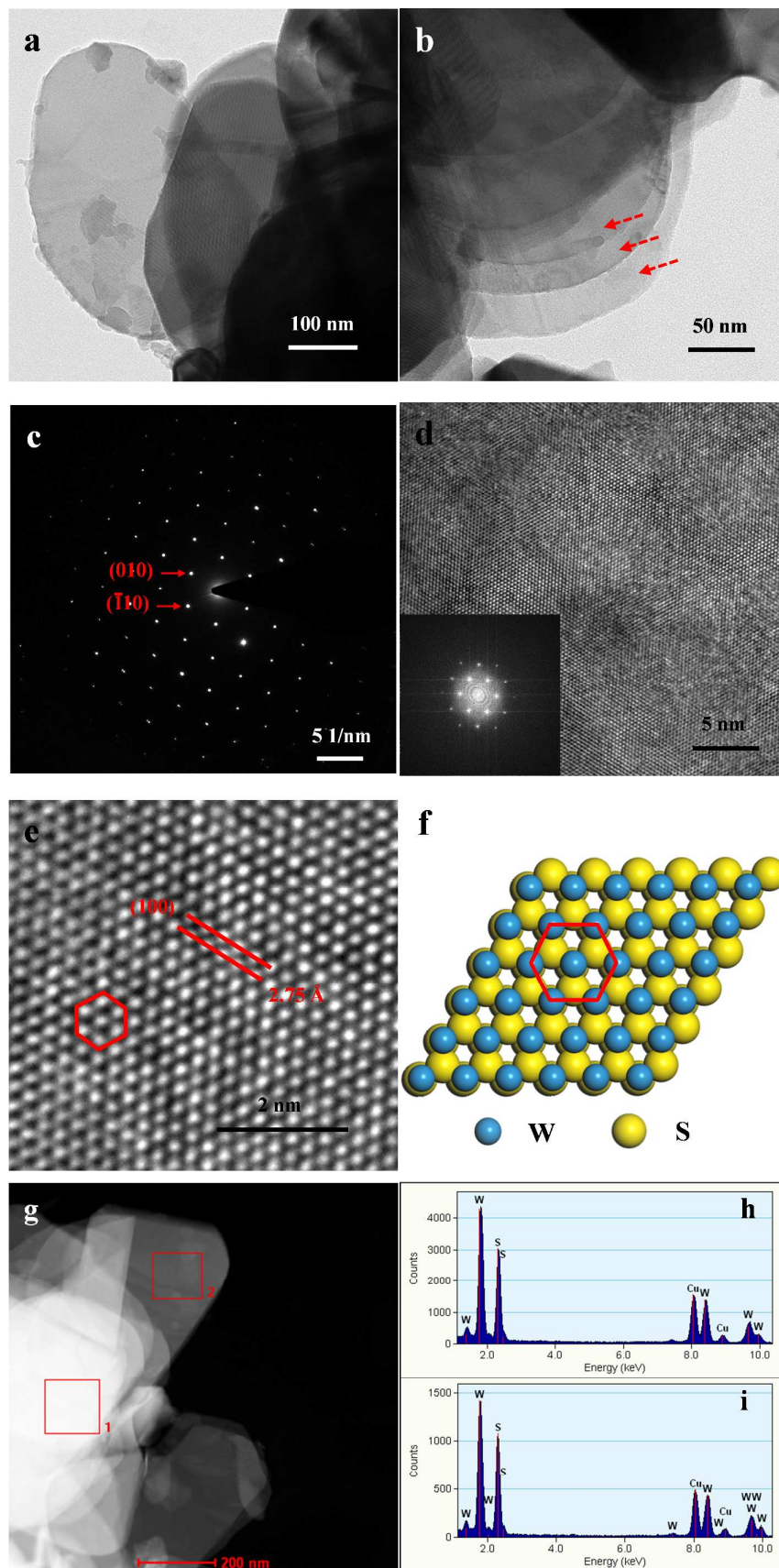


Figure 2. (a, b) Low-magnification TEM images, (c) SAED pattern, and (d, e) HRTEM images of the WS₂ samples. (f) Schematic illustration of plane (002) of WS₂. Inset of (d) shows the FFT pattern corresponding to the HRTEM image. (g) STEM image of the WS₂ nanosheets, and (h, i) NB-EDX spectra corresponding to the marked areas by square 1 and 2 in (g) respectively.

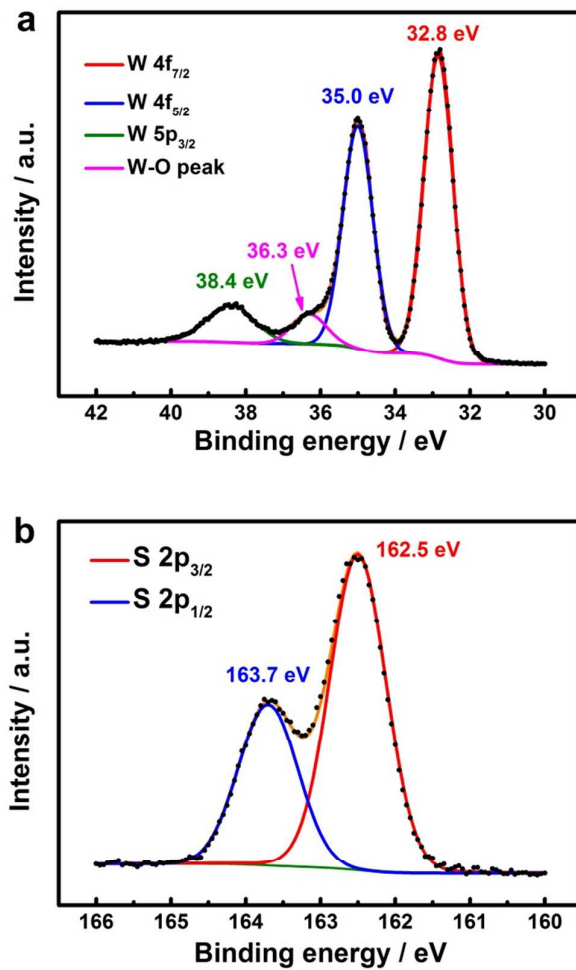


Figure 3. XPS spectra of (a) W 4f and W 5p, and (b) S 2p for the WS₂ nanosheets.

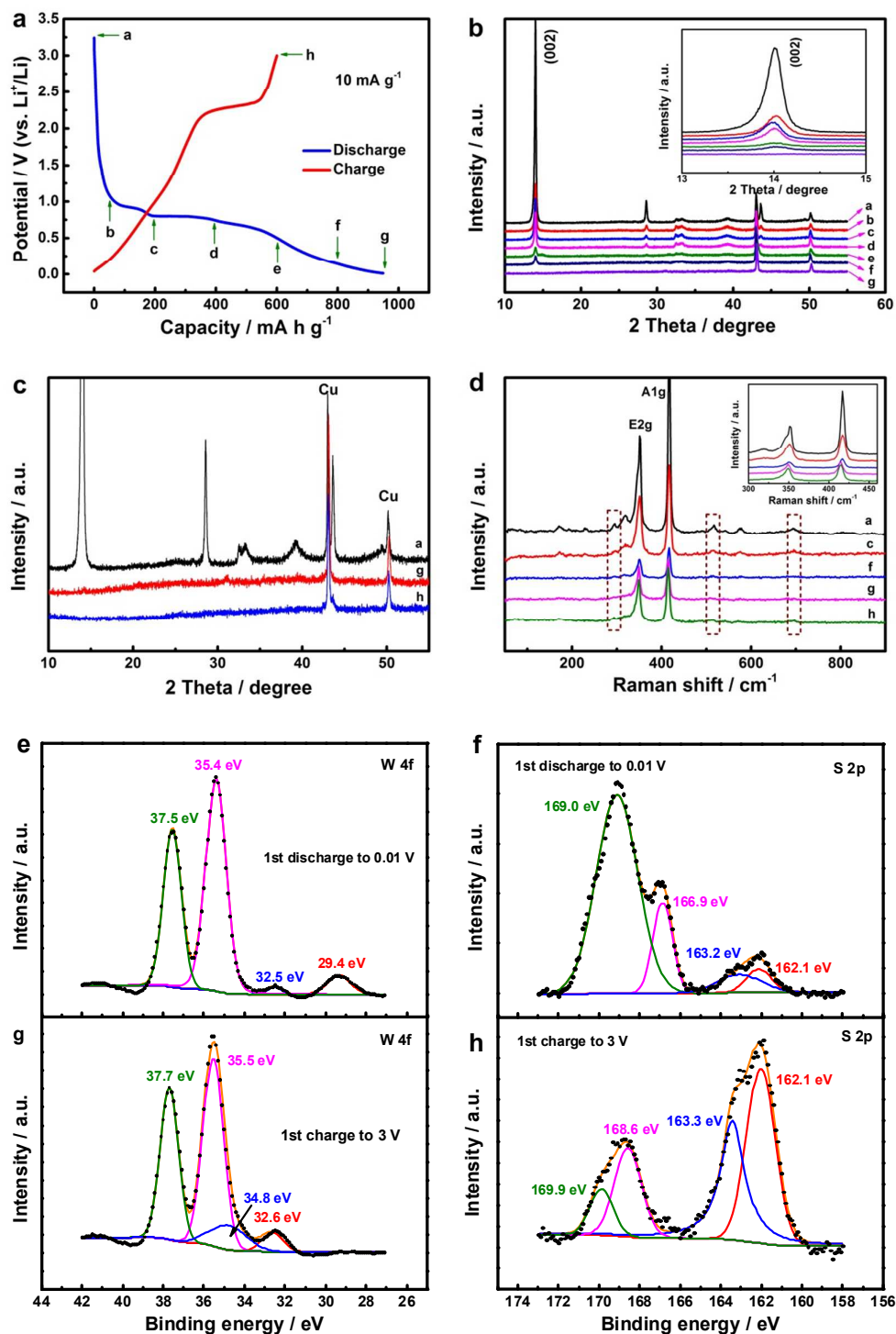


Figure 4. (a) The discharge/charge profiles of the WS₂-nanosheet electrode at 10 mA g⁻¹ between 0.01 and 3.0 V (vs. Li⁺/Li) for the first cycle. The letters “a” to “h” denote the states of different lithiated electrodes for corresponding ex-situ X-ray patterns and

Raman spectra. (b, c) Ex-situ XRD patterns collected at various states from “a” to “h”.
(d) Ex-situ Raman spectra collected at various states of “a”, “c”, “f”, “g” and “h”. (e-h)
XPS spectra of W 4f and S 2p: the electrode film at the state of (e, f) “g” and (g, h)
“h”.

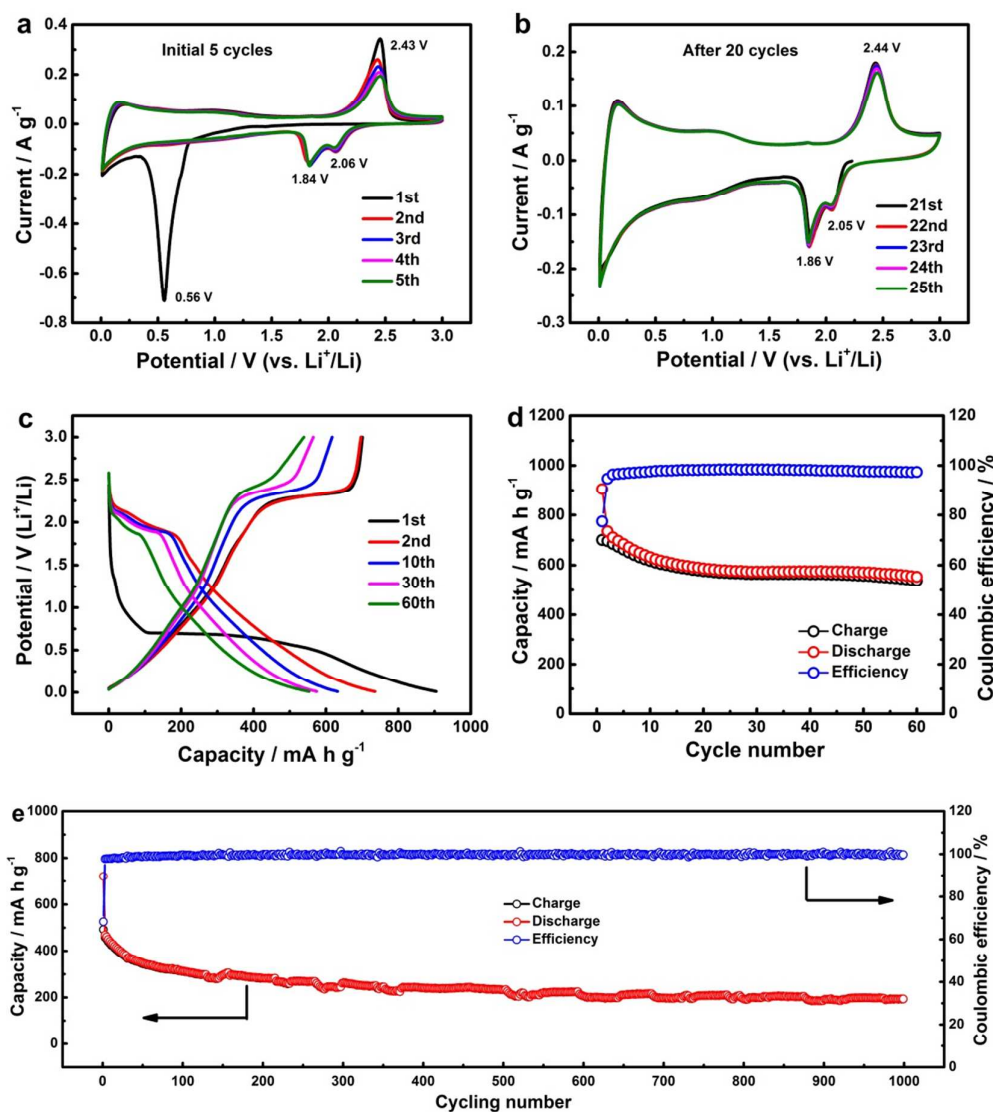


Figure 5. (a, b) Cyclic voltammograms of the WS₂-nanosheet electrode over a potential window of 0.01-3 V (vs. Li⁺/Li) at a scan rate of 0.1 mV s⁻¹ (a) before discharge/charge cycling and (b) after the 20th discharge/charge cycle. (c) Galvanostatic discharge/charge curves of the WS₂-nanosheet electrode at different cycles in a potential range of 0.01-3 V (vs. Li⁺/Li) at a current density of 0.2 A g⁻¹. Cycling performance of the WS₂-nanosheet electrode at current densities of (d) 0.2 A g⁻¹ and (e) 1 A g⁻¹.

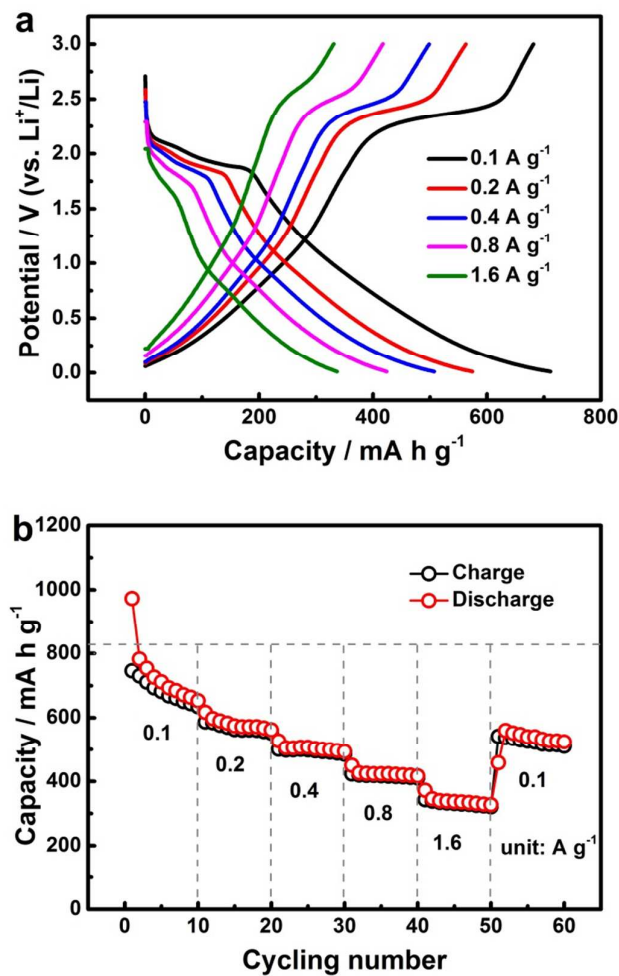


Figure 6. (a) Representative discharge/charge profiles, and (b) rate performance of the WS₂-nanosheet electrode at various current densities.

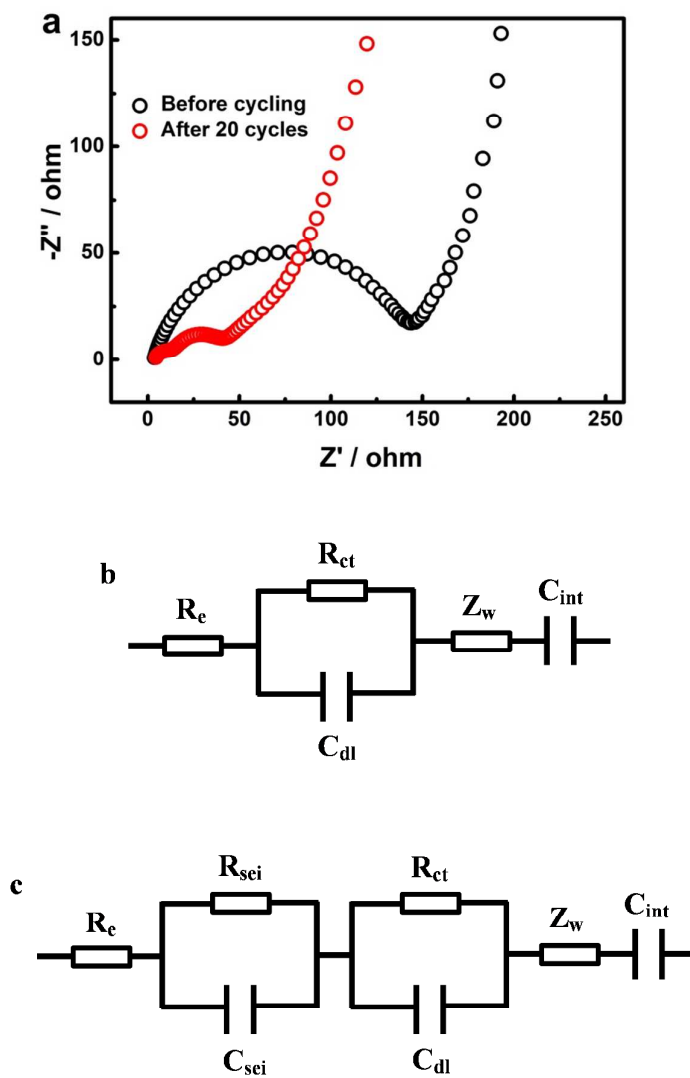
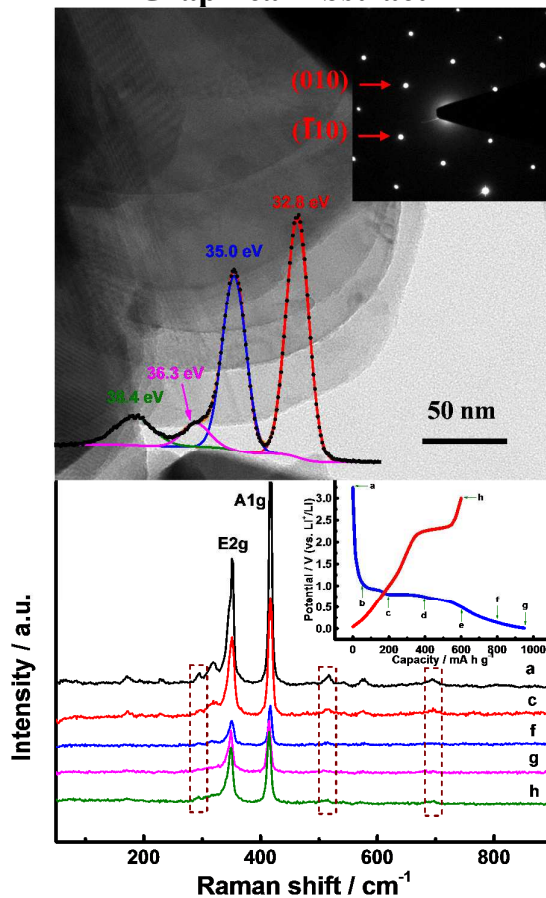


Figure 7. (a) Nyquist plots of the WS₂-nanosheet electrode upon cycling in the charged state (3.0 V vs. Li⁺/Li) over the frequency range of 0.01 Hz-100 kHz. (b, c) Equivalent electrical circuits corresponding to the Nyquist plots (b) before cycling and (c) after the 20th discharge/charge cycle.

Graphical Abstract



Two-dimensional WS₂ nanosheets with preferential orientation of [001] and perfect single crystalline structures exhibit superior lithium storage performance. Ex-situ XRD, Raman and XPS analyses are collected to explore lithium storage mechanism of WS₂ that the recharge product (3.0 V vs. Li⁺/Li) after fully discharging to 0.01 V (vs. Li⁺/Li) tends to reverse metallic W to WS₂.